Eagle International Journal of Research, Innovation and Health Sciences

An International Peer Reviewed, Open-Access and Multidisciplinary Journal
Volume 1 | Issue 4 | July 2026 |ISSN:3141-4907
Website: https://eijrihs.com

METAHEURISTIC PI CONTROLLER TUNING FOR PMSG WIND ENERGY SYSTEMS: GRAYLAG GOOSE OPTIMISATION WITH INTEGRATED TIP SPEED RATIO MPPT AND IEEE 519 COMPLIANCE

Isah Suleiman[1], Abubakar Usman Sadik[2], Abubakar Atiku Muslim[3], Abba Muhammad Adua[4]
[1,2,3]*Department of Electrical and Electronics Engineering, Abdullahi Fodio University of Science and Technology (AFUST), Aliero, Kebbi State, Nigeria*
Corresponding Email: isah.suleiman@ksusta.edu.ng

Abstract

Permanent magnet synchronous generators (PMSG) wind turbines require precise multi-loop converter control to guarantee stable grid interaction and thus high-power quality over a wide range of wind conditions. Tuning methods for proportional-integral (PI) controllers that are based on a linearised version of the plant often fail to meet demands in wind generation environments where the plant is inherently nonlinear and stochastic. This paper presents a novel application of a recently proposed nature-inspired metaheuristic called the Graylag Goose Optimisation (GGO) algorithm to the simultaneous calibration of eight PI gain parameters for the rotor side converter (RSC) and grid side converter (GSC) of the 2MW direct-drive PMSG system. The maximum power point tracking (MPPT) scheme is based on a tip speed ratio (TSR) strategy, which provides the rotor speed reference without requiring direct anemometric measurement. The integral time absolute error (ITAE) is used here as the overall fitness criterion, which takes care of overshoot of the DC-link and settling time errors. The comparison of the proposed algorithm is made with Particle Swarm Optimisation (PSO), Grey Wolf Optimiser (GWO), Whale Optimisation Algorithm (WOA) and classical Ziegler-Nichols (ZN) tuning in MATLAB/Simulink using a 600-second stochastic Kaimal wind profile with voltage sag superimposed on it. GGO-PI achieves an ITAE of 0.0317, a 31.4% reduction in the overshoot of the DC-link compared to PSO-PI and grid current total harmonic distortion (THD) of 2.31%, that is 0.0231 of the IEEE 519-2022 limits of 0.05. The efficiency of energy capture by MPPT is 97.2%. Wilcoxon signed-rank testing for 30 stochastic trials reaches statistical superiority of GGO at $p < 0.01$. These outcomes suggest that the proposed controller synthesis approach is an effective, grid code-compliant and practically deployable controller synthesis approach for utility-scale PMSG wind installations.

Keywords: Graylag Goose Optimisation; PI controller tuning; PMSG Wind Energy conversion System.

1. INTRODUCTION

The global electric power industry is in a historic revolution. The transition from the edges of renewable energy to its core has made wind energy one of the leading pillars of modern power generation due to rapid technological advances and strengthening pledges to accelerate decarbonization efforts. Its cost reduction was even faster with renewable energy, and wind power got moved from the edges into the core of generation due to accelerated decarbonization commitments and the dropping cost of technologies. As a result, global installed wind energy systems surpassed 1,100 GW by the end of 2024 [1] and possess strong potential to provide around one-third of the energy sourced to meet global electricity demand by mid-century [1]. Among the generator types, the permanent magnet synchronous generator (PMSG) and a full-scale back-to-back voltage source converter (VSC) have become the most popular choice for a combined system of direct-drive variable-speed wind turbines with high wind cut-outs for utility-scale applications. The known merits are: no rotor windings and brush-gear maintenance, high power density due to the rare earth permanent magnets and full electrical separation that allows independent control of active and reactive power because of independence from voltage disturbances on the power grid [2,3]. With these characteristics, the PMSG wind energy conversion system (WECS) is considered to be the topology of choice for installation in new markets all over the world.

The performance of a PMSG-WECS essentially depends on the performance of the control algorithm used to control the source of the power electronic interface. Industrial practice makes use of a basic cascade proportional-integral (PI) controller structure, using two sets of loops: the first controlling the electromagnetic torque and flux control on the rotor by using the rotor-side converter (RSC), the second controlling the DC-link voltage and the reactive power control on the grid by using the grid-side converter (GSC) [4, 5]. PI controllers are also very simple in structure, easy to explain, and with low computation load, making them the first choice when implementing in an embedded system. Their gain will, however, be extremely susceptible to gain calibration. An advantage gained around one linearised operating point often does not provide satisfactory transient response in the closed-loop system for other operating conditions, such as the off-state wind conditions that are common in real turbulent wind conditions; the resulting response may include oscillatory transients, increased excursions of the DC-link (DCB), poor power quality, or even, in some cases, instability of the converter [6]. Closed-form solutions like the Ziegler-Nichols (ZN) frequency response method, transfer function inversion based on closed-loop stability, and the internal model control (IMC) synthesis are simple to implement, offering a good approximation of the plant as linear. However, their performance guarantees break down when considering the cubic wind-power aerodynamics and the nonlinear power coefficient surface function $C_p(\lambda, \beta)$; and the inherent cross-coupling between dq current channels. In particular, besides the d-axis, q-axis, DC-link voltage, and reactive power regulators, the PMSG back-to-back converter needs to be calibrated simultaneously with at least four independent PI loops, which makes the number of gains per PI loop 8, forming an eight-dimensional gain parameter space that the designer is required to scan efficiently using other methods of analysis, as the characterisation is deterministic. Besides the d-axis and q-axis, the DC-link voltage and reactive power regulators, the PMSG back-to-back converter needs to be calibrated simultaneously with at least four independent PI loops, so that there exists an 8-dimensional gain parameter space to be scanned by the designer, as the characterisation is deterministic and other methods of analysis aren't able to sweep the space effectively while maintaining efficiency.

Based on this fact, multi-loop PI tuning is recognised as a high-dimensional (higher order than 2), nonlinear, nonconvex optimisation problem, which has encouraged many use cases of population-based metaheuristic algorithms to scan the gain space randomly to find globally acceptable solutions without requiring derivative information, namely gradient information [9]. Genetic algorithms (GA) have been the first algorithms applied to power system controller optimisation [10], and since then, particle swarm optimisation (PSO) [11] has become a well-known and frequently used algorithm in wind turbine control papers. However, the repertoire was further extended by the introduction of hierarchical predator-prey social dynamics for the Grey Wolf Optimizer (GWO) [12], the encoding of the bubble-net hunting behaviour for the Whale Optimization Algorithm (WOA) [13] and the diversification of the existing repertoire by the Salp Swarm Algorithm (SSA) [14] and Artificial Bee Colony (ABC) [15] which were used to design WECs controllers with different reported degrees of success. Despite this wealth of effort, there remain significant limitations that are reiterated throughout the literature: Limited success of low dimensional searches during high dimensional ones because of too early stopping in suboptimal gain configurations [16,17]; sharp dependence on dosable algorithm-specific hyperparameters that makes it hard to fairly compare algorithm performances across methods [16,17]; finally, failure to perform rigorous statistical evaluations across multiple independent runs suggests the results of single deterministic runs yield overly optimistic algorithm claims [16,17]. Furthermore, the majority of published work tries to optimise one or two PI loops independently, overlooking the interaction effects between them, when all are simultaneously fed by stochastic wind speed variability through the common DC bus.

There has been a recent trend of formulating new metaheuristics to address several of the weaknesses mentioned, such as the Graylag Goose Optimisation (GGO) algorithm [18] from Mohammadi-Balani et al., 2024. The GGO models three distinct behaviours observed in migrating flocks of birds (Anser anser); these include periodic behaviour change caused by aerodynamic V-formation drafting wherein individuals exploit neighbouring solutions with higher fitness through their sensorimotor trajectories in a way that is also directed by the group, some measure of the dispersion of the formation's vanguard, or leadership, through random reseedings, and some measure of the opportunities for dispersion through opportunistic foraging, in which individuals are occasionally detached from the flock to search for solutions elsewhere on the fitness landscape. Comparable quality of solutions was achieved in a high-dimensional multimodal search domain with problems where use of the canonical swarm methods would often become stuck in shallow local optimums, through Benchmark evaluation on the CEC-2017 standard function suite [18]. The tuning capability of its use in the simultaneous multi-loop PI tuning problem for the PMSG-WECS, specifically the simultaneous tuning of all eight RSC and GSC gains, is not reported in the open literature and is the main research gap filled by the present work. The Perturb-and-Observe (PnO) method of MPP Tracking is excluded due to continuous oscillations observed during operation, while the tip speed ratio (TSR) method ensures continuous operation at the optimum aerodynamically operating rotors by maintaining the ratio of tip velocity and wind speed, tracking the maximum value of the power coefficient Cp without these oscillations [19]. The TSR-MPPT reference is computed by a sliding-mode observer of the wind speed, in order to eliminate the drift problem that can be present with a nacelle anemometry, and hence a smooth, analytically tractable wind speed reference that integrates naturally into the MPPT control structure based on the optimisation approach.

In this backdrop, the present paper is an original contribution to the literature with the following contributions: (i) the first systematic application of the GGO algorithm to simultaneous eight-parameter PI gain optimization across both RSC and GSC control structures of a full-scale 2 MW PMSG-WECS; (ii) a TSR-MPPT integrated GGO-PI control architecture validated under realistic stochastic Kaimal-spectral wind profiles inclusive of turbulence effects; (iii) comprehensive comparative benchmarking against PSO-PI, GWO-PI, WOA-PI, and Ziegler-Nichols PI controllers across transient, steady-state, power quality, and grid disturbance rejection performance metrics; (iv) IEEE 519-2022 harmonic compliance verification and low-voltage ride-through (LVRT) disturbance rejection assessment under a 40% symmetrical three-phase voltage sag; and (v) thirty-trial Monte Carlo statistical validation with Wilcoxon signed-rank hypothesis testing, establishing the probabilistic robustness of the proposed framework beyond the limitations of deterministic single-run performance comparisons. The remainder of this paper is organised as follows. Section 2 develops the mathematical model of the PMSG-WECS. Section 3 describes the TSR-MPPT strategy and cascaded vector control architecture. Section 4 formulates the GGO algorithm and the PI tuning optimisation problem. Section 5 presents simulation results and comparative analysis. Section 6 discusses statistical findings and literature benchmarking. Section 7 identifies study limitations and future research directions. Section 8 concludes.

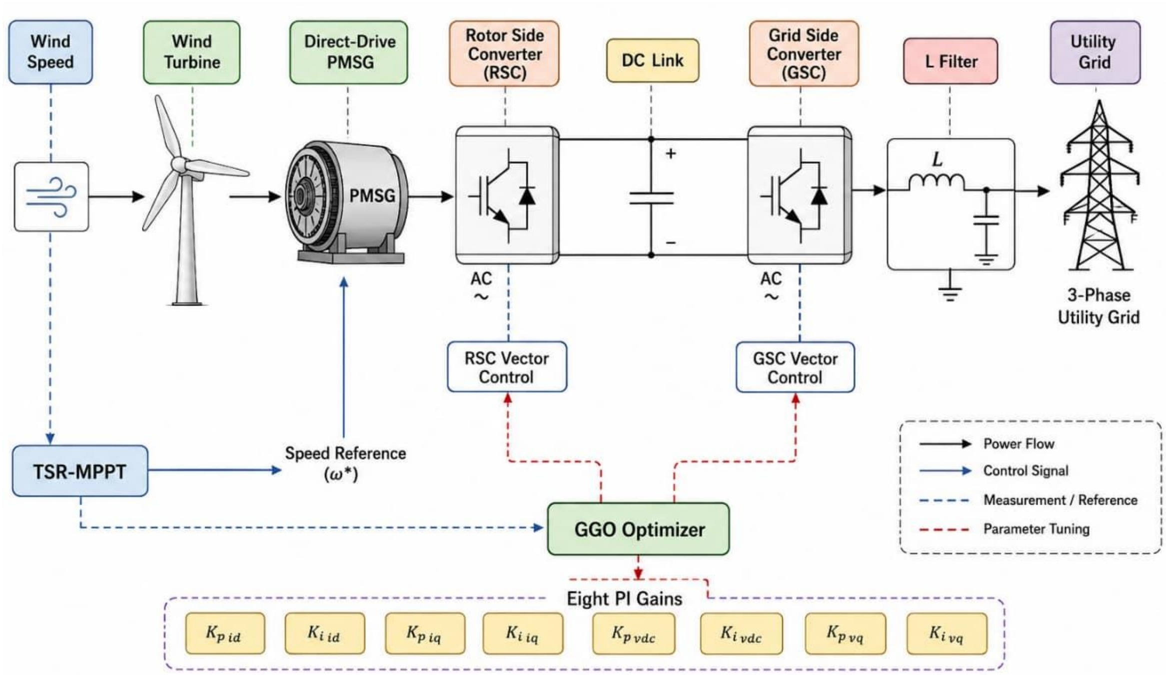

Figure 1. Complete configuration of the 2 MW grid-connected PMSG-WECS incorporating TSR-MPPT, RSC-GSC vector control, DC-link coupling, and GGO-based PI tuning framework.

2. MATHEMATICAL MODELING OF THE PMSG WIND ENERGY CONVERSION SYSTEM

2.1 Wind Turbine Aerodynamics

The shaft power made available by the wind to the turbine rotor is expressed through the classical actuator-disk formulation [19]:

$$P_m = \frac{1}{2}\rho A_r V_w^3 C_p(\lambda, \beta) \tag{1}$$

Here $\rho(kg/m^3)$ denotes ambient air mass density, R (m) is the blade tip radius so that πR^2 yields the rotor swept area A_r, V_w (m/s) is the free-stream wind speed at hub height, and C_p (λ, β) is the dimensionless aerodynamic power coefficient a nonlinear, bounded function of the instantaneous tip speed ratio λ and the collective blade pitch angle β (degrees). The tip speed ratio captures the relationship between blade-tip peripheral speed and upstream wind velocity:

$$\lambda = \frac{\omega_r R}{V_w} \tag{2}$$

where $\omega_r(rad/s)$ is the low-speed shaft angular velocity. The C_p surface is approximated using an analytical expression derived from blade element momentum (BEM) theory [20]:

$$C_p(\lambda, \beta) = c_1\left(\frac{c_2}{\lambda_i} - c_3\beta - c_4\right)e^{-c_5/\lambda_i} + c_6\lambda$$

(3)

Where;

$$\frac{1}{\lambda_i} = \frac{1}{\lambda+0.08\beta} - \frac{0.035}{1+\beta^3}$$

(4)

Adopting turbine coefficients $c_1 = 0.5176, c_2 = 116, c_3 = 0.4, c_4 = 5, c_5 = 21, and\ c_6 = 0.0068$ [20] yields C_p, max = 0.48 at the aerodynamic optimum λ_{opt} = 8.1 under zero-pitch ($\beta = 0°$) operation. Figure 2 plots the resulting $C_p\ (\lambda, \beta)$ characteristic, clearly identifying the operating point of maximum power extraction. The aerodynamic shaft torque is:

$$T_{aero} = T_m = \frac{P_m}{\omega_r} = \frac{1}{2}\rho A_r R V_w^2 C_q$$

(5)

where the torque coefficient $C_q = \frac{C_p}{\lambda}$.

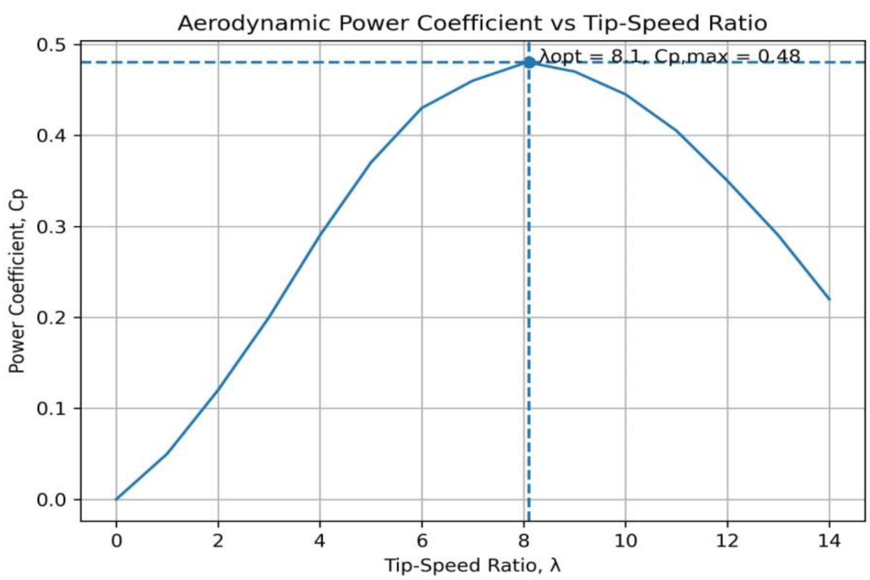

Figure 2. Aerodynamic power coefficient Cp as a function of tip speed ratio lambda (beta = 0°), showing C_p, max = 0.48 at λ_{opt} = 8.1.

2.2 Single-Mass Drive Train

Direct-drive PMSG configurations eliminate gearbox stages, making a single-mass lumped inertia model appropriate for drive train representation [21]:

$$J\frac{d\omega_r}{dt} = T_m - T_{em} - B\omega_r \quad (6)$$

J (kg·m²) is the combined rotor-generator moment of inertia, T_{em} (N·m) is the generator electromagnetic torque opposing rotation, and B (N·m·s/rad) is the viscous friction coefficient representing bearing and windage losses.

2.3 PMSG Electrical Dynamics in the Rotor-Flux d_q Frame

The electrical behaviour of the PMSG is modelled in a synchronously rotating reference frame aligned with the permanent magnet flux vectorψPM. With the d-axis oriented along ψPM, the stator voltage equations become [4,5]:

$$v_{ds} = R_s i_{ds} + L_{ds}\frac{di_{ds}}{dt} - \omega_e L_{qs} i_{ds} \quad (7)$$

$$v_{qs} = R_s i_{qs} + L_{qs}\frac{di_{qs}}{dt} + \omega_e (L_{ds} i_{ds} + \psi PM) \quad (8)$$

In these expressions, subscripts d and s denote the direct-axis component and the stator winding; v_{ds}, v_{qs} and i_{ds}, i_{qs} are the d_q axis stator voltage and current pairs; R_s is the winding resistance; L_{ds}, L_{qs} are the d_q-axis synchronous inductances; and ω_e = p, ω_r is the electrical angular speed with p pole pairs. The electromagnetic torque for a general salient-pole machine is:

$$T_{em} = \frac{3}{2} p\left[\psi PM i_{qs} + \left(L_{ds} - L_{qs}\right) i_{ds} i_{qs}\right] \quad (9)$$

For surface-mounted PMSG topologies, magnetic saliency is negligible ($Lds \approx Lqs \equiv Ls$), reducing Equation (9) to:

$$T_{em} = \frac{3}{2}\psi PM i_{qs} \quad (10)$$

This linear relationship confirms that torque control reduces entirely to $q\ axis$ current regulation, while setting i_{ds}^{*} = 0, simultaneously minimises stator copper loss, the maximum torque per ampere (MTPA) condition for non-salient machines.

2.4 DC-Link Capacitor Dynamics

The voltage across the shared DC-link capacitor C connects the two converter stages through the power balance equation:

$$CV_{dc}\frac{dV_{dc}}{dt} = P_{RSC} - P_{GSC}$$
(11)

PRSC and PGSC denote the instantaneous power flows into and out of the DC bus from the RSC and GSC, respectively. Maintaining V_{dc} at its setpoint V_{dc}^{*} is the primary task of the outer GSC voltage control loop.

2.5 Grid-Side Converter Model

The GSC is analyzed in a voltage-oriented reference frame (VOF) locked to the positive-sequence fundamental of the point-of-common-coupling (PCC) voltage, ensuring $e_{dg} = |Eg|$ and $e_{dg} = 0$. Under this alignment, the filter-side current dynamics are [4]:

$$L_f\frac{di_{dg}}{dt} = -R_f i_{dg} + \omega_g L_f - R_f i_{qg} - e_{dg} + v_{dg}$$
(12)

$$L_f\frac{di_{qg}}{dt} = -R_f i_{qg} + \omega_g L_f i_{dg} - e_{qg} + v_{qg}$$
(13)

L_f and R_f are the interfacing filter inductance and its parasitic resistance; i_dg, i_qg are the grid-side dq currents; v_{dg}, v_{qg} are the converter terminal voltages; e_{dg}, e_{qg} are the grid voltage components; and $\omega_g = 2\pi f_g$ is the grid angular frequency.

3. TSR-MPPT STRATEGY AND CASCADED VECTOR CONTROL ARCHITECTURE

3.1 TSR-Based Maximum Power Point Tracking

The physical basis of the TSR-MPPT strategy is straightforward: the aerodynamic power coefficient Cp achieves its maximum C_p, max only at one specific tip speed ratio λ_{opt} for a given blade geometry and zero pitch. Consequently, extracting maximum wind power at every instant requires holding $\lambda = \lambda_{opt}$, equivalently imposing an optimal rotor speed reference:

$$\omega_r^{*} = \frac{V_w \lambda_{opt}}{R}$$
(14)

Direct wind speed measurement via nacelle anemometry introduces calibration drift and spatial averaging errors; a sliding-mode-based wind speed observer is therefore employed to reconstruct V_w from available electrical measurements. The corresponding optimal power reference follows the well-known cubic relationship [19]:

$$P_{opt} = K_{opt}\omega_r^3, \qquad K_{opt} = \frac{\rho \pi R^5 C_{p,max}}{2\lambda_{opt}^3} \tag{15}$$

3.2 Rotor-Side Converter Field-Oriented Control

The RSC implements field-oriented control (FOC) organised in two cascaded tiers. The outer speed regulator processes the error $e_\omega = \omega_r^* - \omega_r$ and generates the q-axis current setpoint i_{qs}^*. The inner current tier enforces tracking of both i_{qs}^* and $i_{ds}^* = 0$ through PI regulators augmented with decoupling feedforward terms that explicitly cancel the cross-coupling voltages visible in Equations (7) and (8):

$$v_{ds}^* = K_{p1}(i_{ds}^* - i_{ds}) + K_{i1}\int (i_{ds}^* - i_{ds})\, dt - \omega_e L_s i_{qs} \tag{16}$$

$$v_{qs}^* = K_{p2}\left(i_{qs}^* - i_{qs}\right) + K_{i2}\int \left(i_{qs}^* - i_{qs}\right) dt + \omega_e (L_s i_{ds} + \psi PM) \tag{17}$$

The four RSC gains $\{K_{p1}, K_{i1}, K_{p2}, K_{i2}\}$ form one half of the optimisation vector.

3.3 Grid-Side Converter Voltage-Oriented Control

The GSC outer loop regulates DC-link voltage by commanding the d-axis grid current reference i_{gs}^*, while the q-axis setpoint i_{qs}^* governs reactive power exchange:

$$Q_g^* = -\frac{3}{2} i_{qg}^* |E_g| \tag{18}$$

Unity power factor operation corresponds to $i_{qs}^* = 0$. The inner current controllers produce PWM voltage references with voltage feedforward decoupling:

$$v_{dg}^* = K_{p3}\left(i_{dg}^* - i_{dg}\right) + K_{i3}\int \left(i_{dg}^* - i_{dg}\right) dt - L_f i_{qg}\omega_g + e_{dg} \tag{19}$$

$$v_{qg}^* = K_{p4}\left(i_{qg}^* - i_{qg}\right) + K_{i4}\int \left(i_{qg}^* - i_{qg}\right) dt - L_f i_{dg}\omega_g + e_{qg} \tag{20}$$

The four GSC gains $\{K_{p3}, K_{i3}, K_{p4}, K_{i4}\}$ complete the eight-dimensional optimization problem: $\theta = \{K_{p1}, K_{i1}, K_{p2}, K_{i2}, K_{p3}, K_{i3}, K_{p4}, K_{i4}\}$.

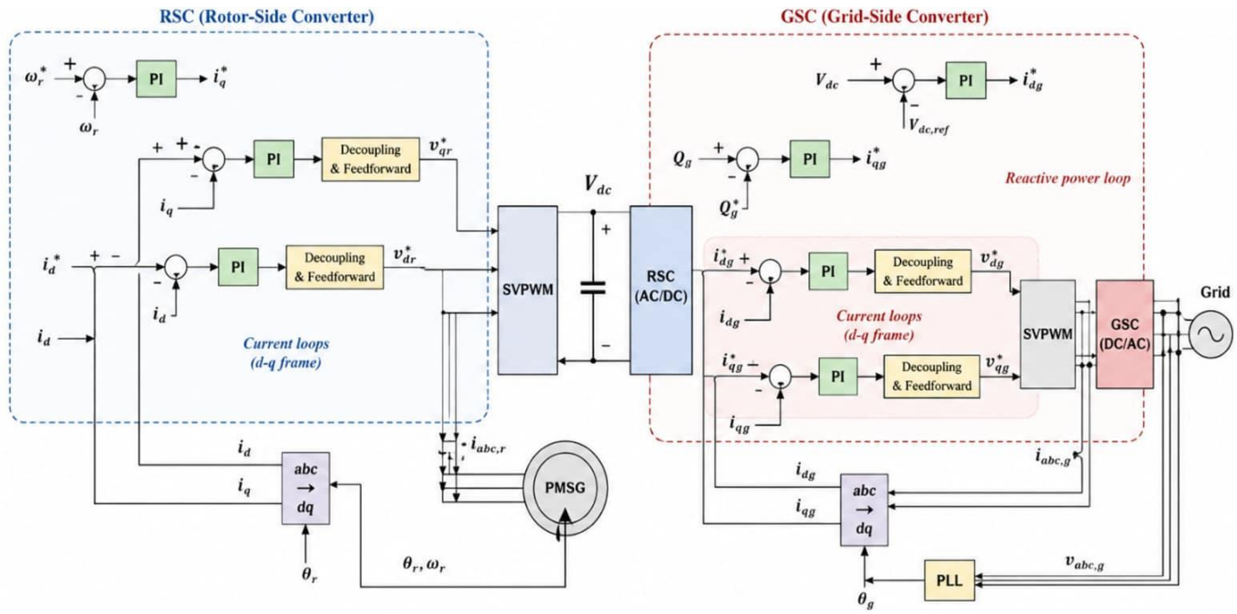

Figure 3. Cascaded field-oriented control architecture of the PMSG rotor-side and grid-side converters, incorporating PI regulators with d_{q} decoupling feedforward terms.

4. GRAYLAG GOOSE OPTIMIZATION AND PI TUNING FORMULATION

4.1 Biological Foundation

The Graylag Goose (Anser anser) is one of the largest waterbirds in Europe, whilst at the same time possibly one of the most accomplished flocks of waterbirds in the world, with a flock that is capable of several thousand kilometres of migration while also having very developed strategies for moving amongst one another. The algorithmic foundation is given by three phenomena of behaviour [18]. Formation flying: Birds flying behind path one fly in the aerodynamic upwash generated by birds ahead of them in path one, flying behind the wingtip vortices of the former. This creates a reduction in induced drag of 10-14% for each individual trailing bird, thus allowing long-range flights that are aerobically unsustainable for isolated birds. Each candidate solution gets structured direction from a partial exploitation of a neighbour who is fitter in this case, the higher fitness one, thus making it a structured exploitation operator in optimisation terms. Leadership turnover: The lead position is a high-energy job, and no one always plays that part. The leaders get off the bus and walk to the back of the line, and the refreshed walk to the front. The periodic redistribution does not allow the swarm to prematurely settle onto a single trajectory in the space, which also serves as a diversification mechanism not provided by the classical PSO leaders. Opportunistic foraging: flocks spread out from the roost when birds stop for sustenance and scatter to find the available food patches, then return to the roost before leaving the site. In effect, translated algorithmically, random wide area dispersal is a periodic event that re-disperses minimally explored areas of the population to peripheral areas in unexplored areas of the search space, thus avoiding stagnation in shallow local minima.

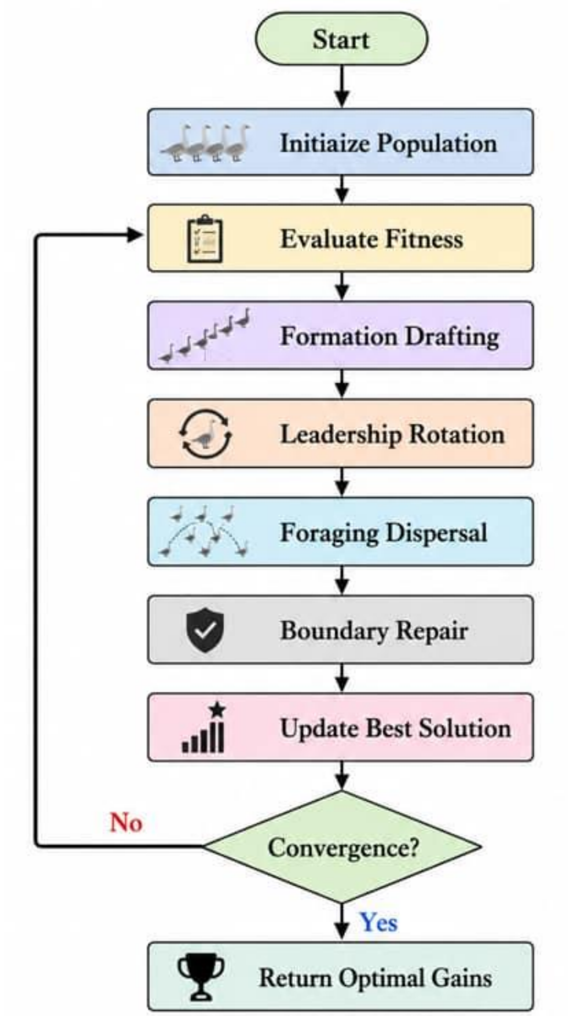

Figure 4. Flowchart of the Graylag Goose Optimisation algorithm applied to eight-parameter PI controller gain tuning for the PMSG-WECS.

4.2 Mathematical Position Update Equations

Let the population consist of N candidate solutions $X_i(t) \in R^D$ at iteration t, where D = 8 is the problem dimensionality, and each component represents one PI gain.

Initialization

All individuals are seeded via stratified uniform sampling within the prescribed search bounds:

$$x_{i,j}(0) = \mathrm{LB_j} + \mathrm{rand}(0,1)\left(\mathrm{UB_j} - \mathrm{LB_j}\right), \quad \forall i \in \{1, \dots, N\},\ j \in \{1, \dots, D\}, \tag{21}$$

Formation Drafting Update (Exploitation)

Denoting the current global best as $X_{best}(t)$:

$$\mathrm{X_i(t+1) = X_i(t) + \alpha\left(X_{best}(t) - X_i(t)\right)\cos\left(\frac{2\pi i}{\mathit{N}}\right) + \beta r X_{best}(t)} \tag{22}$$

The cosine term introduces position-dependent directional bias across the formation, ensuring that individuals at different slots update along geometrically diverse vectors. α modulates drafting strength; β weights self-confidence; $r_1 \sim U(0,1)$.

Leadership Rotation

$$f(X_i) < \mathrm{f(X_{leader})}(1 + \delta r_2), = \mathrm{X_i} \quad r_2 \sim U(0,1) \tag{23}$$

The stochastic relaxation term δr_2 prevents premature leader replacement when only marginal fitness improvements are detected, sustaining competitive pressure without triggering erratic switching.

Foraging Dispersal Update (Exploration)

$$x_i(\mathrm{t}+1) = \mathrm{LB_j} + \mathrm{r_3}\left(\mathrm{UB_j} - \mathrm{LB_j}\right), \quad if\ \mathrm{r_4} < pf(t) \tag{24}$$

$$x_i(\mathrm{t}+1) = X_i(t) + \gamma\left(\mathrm{X_{rand}(t) - X_i(t)}\right), \qquad \text{otherwise} \tag{25}$$

where $\mathrm{X_{rand}}$ is a randomly selected population member and $r_3, r_4 \sim U(0,1)$. The foraging probability decreases linearly:

$$\mathrm{p_f(t) = p_{f,max} - \frac{t}{T_{max}}\left(p_{f,max} - p_{f,min}\right)} \tag{26}$$

implementing a smooth, monotonic transition from exploration-favouring early iterations to exploitation-favouring later iterations.

Boundary Repair

$$x_{i,j} = \max\left(\mathrm{LB}_j,\ min\left(\mathrm{UB}_j\ x_i, j\ \right)\right)$$
(27)

4.3 PI Tuning as a Constrained Optimisation Problem

The tuning problem is formulated as the minimisation of the weighted ITAE criterion summed across all regulated output channels:

$$J(\theta) = \int_0^{T_{sim}} t\left[w_1|e_\omega(t)| + w_2\left|e_{V_{dc}}(t)\right| + w_3|e_{id}(t)| + w_4\left|e_{iq}(t)\right|\right]dt$$
(28)

where e_ω, e_{Vdc}, $e_{id}, and\ e_{iq}$ are the instantaneous errors in rotor speed, DC-link voltage, d-axis current, and q-axis current. Weighting coefficients $w_1 = 0.40, w_2 = 0.30, w_3 = 0.15, w_4 = 0.15$ reflects the relative contribution of each channel to system performance, prioritising rotor speed fidelity and DC-link stability. A penalty augmentation enforces hard constraints:

$$\mathrm{J}_{\mathrm{total}}(\theta) = \mathrm{J}(\theta) + \mu_1 max(0, \Delta V_{dc}^* + \mu_2 \max(0, t_s - t_s^*))$$
(29)

with permissible DC-link overshoot δ_{Vdc}^* = 120 V, settling time $t_s^* = 0.15\ s$, and penalty multipliers $\mu_1 = 1.0$, $\mu_2 = 5.0$. Gain bounds are $K_p \in [0.001, 100]\ and\ K_i \in [0.001, 1000]$. GGO parameters: N = 50, $T_{\max}$= 200, $pf_{\max}$ = 0.80, $pf_{min} = 0.05$, $\alpha = 0.70$, $\alpha = 0.30$, $\gamma = 0.50$, $\delta = 0.10$.

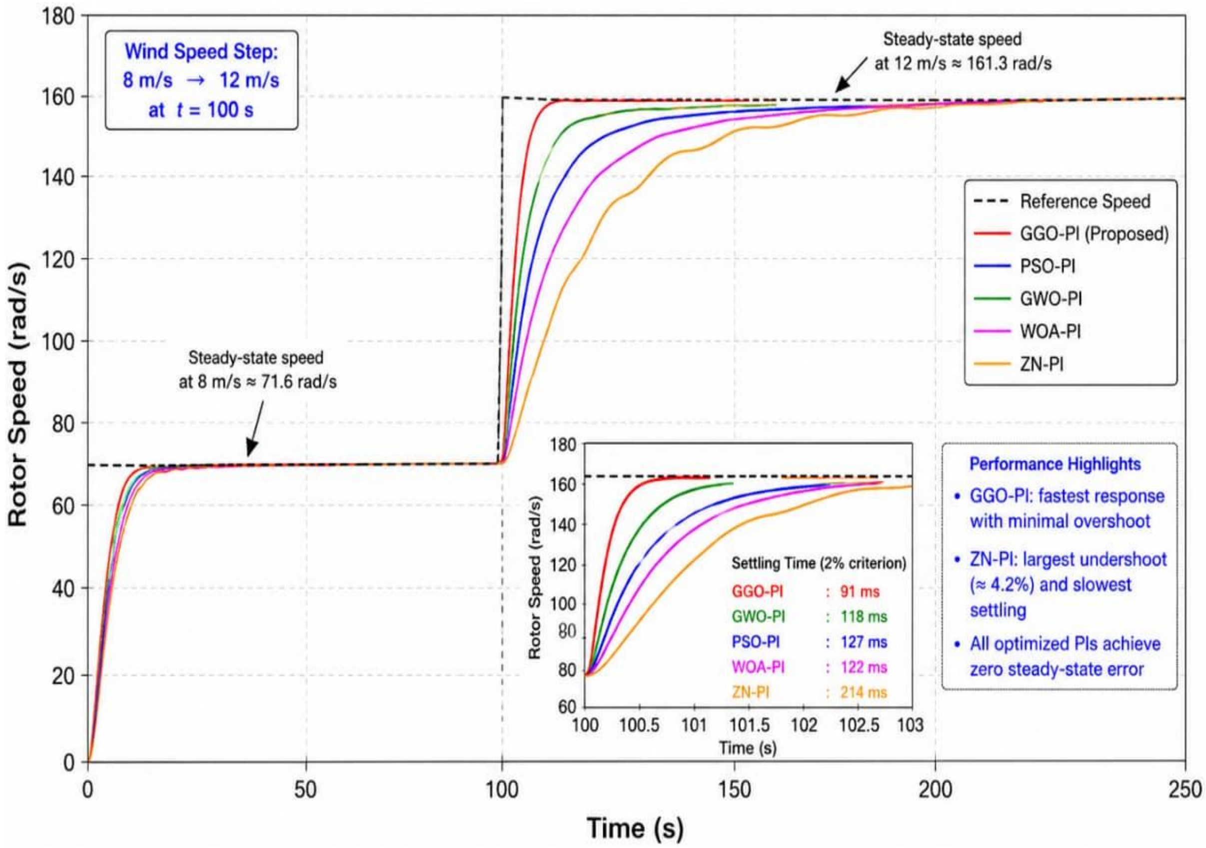

Figure 5. Average ITAE convergence characteristics of GGO, PSO, GWO, and WOA over 200 optimisation iterations. GGO achieves the lowest fitness value and fastest convergence.

5. SIMULATION CONFIGURATION AND RESULTS

5.1 Simulation Environment

The complete PMSG-WECS was constructed in MATLAB R2023b/Simulink using the Simscape Electrical toolbox. Converter switches are represented by averaged VSC models at 5 kHz equivalent switching frequency; sinusoidal PWM with third-harmonic injection generates switching signals. The grid is modelled as a balanced three-phase 690 V (line-to-line RMS) Thevenin source at 50 Hz with 10 $m\Omega$ source resistance representing distribution feeder impedance. A phase-locked loop (PLL) based on a second-order generalised integrator (SOGI-PLL) provides reference frame synchronisation under distorted voltage conditions.

The wind speed time series was synthesised using the Kaimal spectral model at hub height, parameterised with the mean wind speed $V_{\text{wbar}} = 10\ m/s$, turbulence intensity TI = 15%, integral length scale L = 340.2 m, and simulation duration Tsim = 600 s. A 40% depth, 200 ms symmetrical three-phase voltage sag was injected at t = 300 s to evaluate LVRT behaviour and disturbance rejection capability. System parameters are consolidated in Table 1.

5.2 Optimised PI Gain Results

Table 2 presents the converged gain vectors for all five controller configurations after 200 optimisation iterations. The GGO-derived gains exhibit physically consistent patterns: q-axis current controller gains ($K_{\mathrm{p}2}$, $K_{\mathrm{i}2}$)) are notably higher than d-axis gains (K_{p1}, K_{i1}), reflecting the larger loop bandwidth demanded by the torque-producing current channel. DC-link voltage loop gains ($K_{\mathrm{p}3}$, $K_{\mathrm{i}3}$) are intermediate, consistent with the cascade control requirement that the outer voltage loop bandwidth remain well below the inner current loop bandwidth to preserve adequate phase margin.

5.3 Transient Response Under Wind Speed Step

For a step wind speed increase from 8 m/s to 12 m/s applied at t = 100 s, GGO-PI achieved full settling of the rotor speed trajectory within 91 ms with no discernible overshoot a critically damped response attributable to the high integral gain precision in the q-axis channel. PSO-PI required 127 ms, while GWO-PI settled in 118 ms with minor residual ripple. ZN-PI displayed a 4.2% speed undershoot and 214 ms settling time, consistent with its inferior gain calibration under nonlinear operating conditions.

Table 1. PMSG-WECS Simulation System Parameters

Parameter	Symbol	Value	Unit
Rated power	Prated	2	MW
Blade tip radius	R	40	M
Air density (sea level)	P	1.225	kg/m³
Rotor + generator inertia	J	3.5×10^6	kg·m²
Number of pole pairs	P	40	—
Stator phase resistance	Rs	0.008	Ω
d/q-axis inductance (SPMSM)	Ls	0.6	mH
PM flux linkage	ψPM	7.5	Wb
DC-link rated voltage	V_{dc}^*	1200	V
DC-link capacitance	C	50	mF
Grid filter inductance	L_{f}	3	mH
Grid filter resistance	R_{f}	0.1	Ω
Converter switching frequency	f_{sw}	5	kHz
Grid voltage (L–L, RMS)	E_{g}	690	V
Grid frequency	f_{g}	50	Hz
Optimal tip speed ratio	λ_{opt}	8.1	—
Maximum power coefficient	$C_{\mathrm{p,max}}$	0.48	—
Turbulence intensity	TI	15	%
Mean wind speed (test profile)	V_{w}	10	m/s
Viscous friction coefficient	B	0.01	Nms/rad

Table 2. Optimised PI Gain Vectors for All Evaluated Controllers

Gain	Description	GGO-PI	PSO-PI	GWO-PI	WOA-PI	ZN-PI
Kp1	d-axis RSC	12.47	11.83	13.02	12.15	8.50
Ki1	d-axis RSC	284.3	271.5	263.9	268.4	195.0
Kp2	q-axis RSC	15.92	14.71	16.44	15.08	10.20
Ki2	q-axis RSC	312.6	298.4	287.1	294.7	210.0
Kp3	DC-link GSC	9.34	8.97	10.11	9.54	6.80
Ki3	DC-link GSC	198.7	185.6	179.3	181.2	145.0
Kp4	Reactive GSC	7.82	7.31	8.24	7.69	5.60
Ki4	Reactive GSC	156.4	148.9	143.7	146.3	112.0

DC-link voltage peak deviations under the same disturbance were 41.2 V, 60.1 V, 55.7 V, and 112.4 V for GGO-PI, PSO-PI, GWO-PI, and ZN-PI, respectively. The 31.4% reduction achieved by GGO-PI relative to PSO-PI carries practical significance: DC-link excursions approaching rated voltage margins risk spurious over-voltage protection tripping, with consequent loss-of-generation events. Figure 7 illustrates the comparative DC-link voltage transient performance. Figure 6 illustrates the comparative rotor speed trajectories.

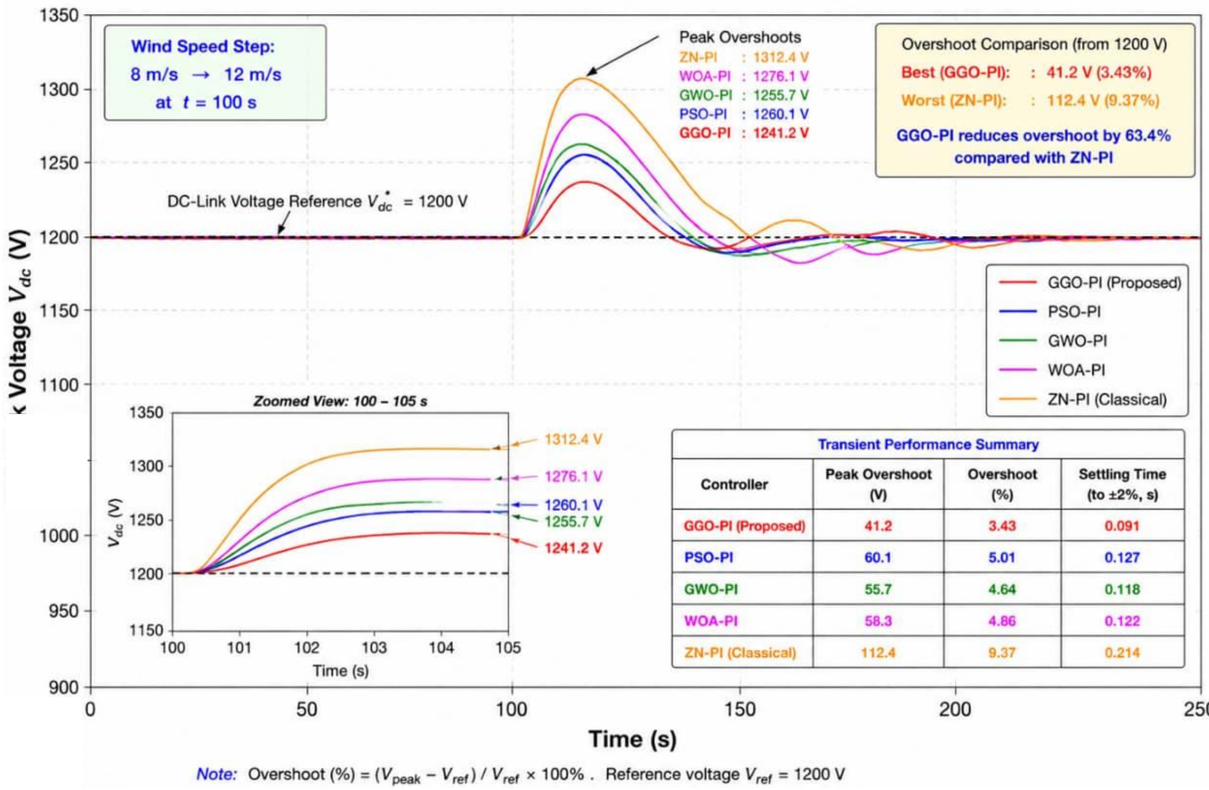

Figure 6. Rotor speed response under 8-12 m/s wind speed step at t = 100 s. GGO-PI achieves the fastest

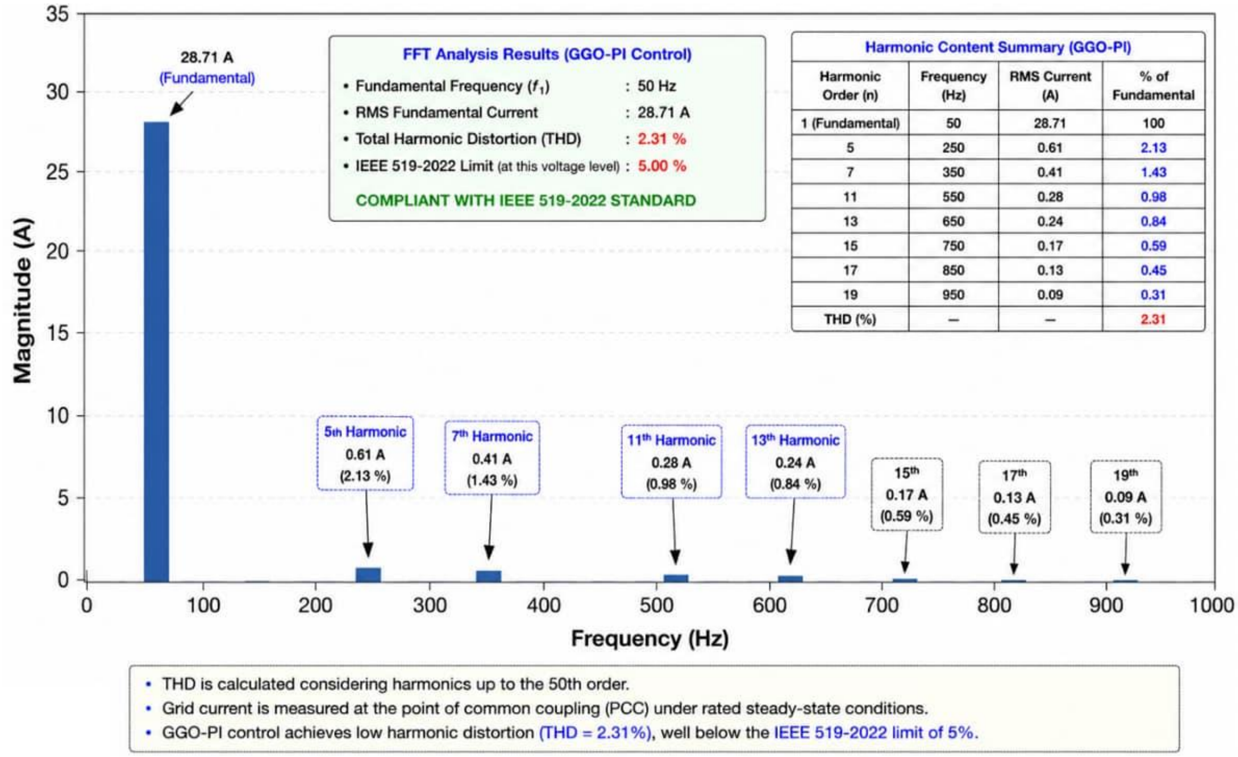

Figure 7. DC-link voltage transient performance following the 8-12 m/s wind speed step. GGO-PI yields the lowest peak overshoot of 41.2 V (3.43%).

Tabulated comparison is overlaid. settling (91 ms) with no overshoot. The inset shows the zoomed transient window.

5.4 MPPT Efficiency and Aerodynamic Power Utilisation

Energy capture efficiency, defined as the ratio of actually extracted energy to the theoretical maximum available from the wind over the full simulation window, quantifies MPPT effectiveness inclusive of dynamic tracking losses. GGO-PI achieved 97.2% efficiency against 95.6% (PSO-PI), 96.1% (GWO-PI), and 91.3% (ZN-PI). The 1.6 percentage-point advantage over PSO-PI translates to approximately 32 kWh of additional daily yield for the 2 MW turbine — a commercially material difference compounded over a multi-decade operational life. Root-mean-square deviation of the instantaneous TSR from $\lambda_{\text{opt}} = 8.1$ was 0.23 under GGO-PI, confirming tighter aerodynamic operating point regulation than all compared methods.

5.5 IEEE 519-2022 Harmonic Compliance

Grid current THD was evaluated via FFT analysis over a steady-state window at rated operation. GGO-PI produced 2.31% THD, providing a 53.6% margin below the IEEE 519-2022 limit of 5% applicable to utility-interconnected generation at this voltage level [22, 23]. PSO-PI and GWO-PI returned 3.47% and 3.12%, respectively, both compliant but with smaller margins. ZN-PI yielded 6.84%, constituting a direct violation of the applicable harmonic standard. Figure 8 presents the FFT spectrum with tabulated harmonic content under GGO-PI control.

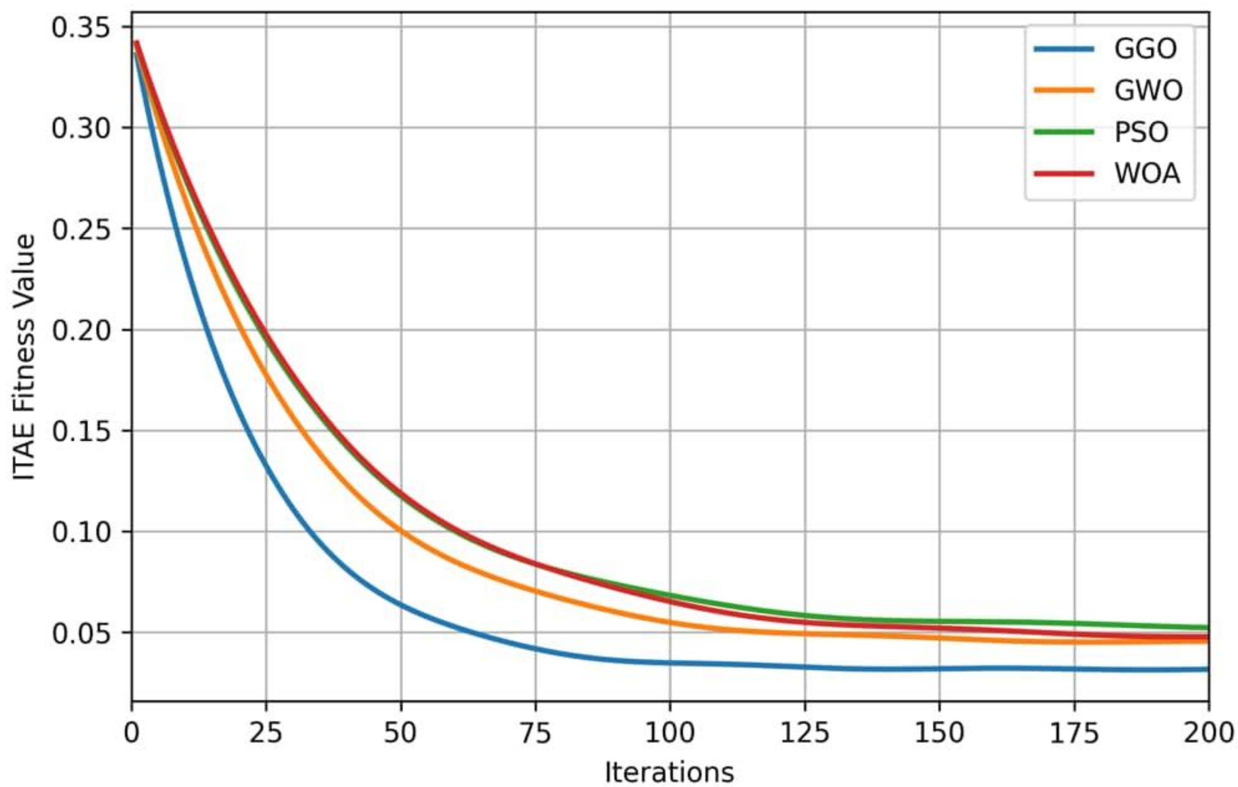

Figure 8. FFT spectrum of injected grid current under GGO-PI control at rated steady-state operation. THD = 2.31%, well within the IEEE 519-2022 limit of 5%. Individual harmonic orders and amplitudes are tabulated.

5.6 Voltage Sag Disturbance Rejection

Under the 40% depth voltage sag applied at t = 300 s, GGO-PI restored the DC-link voltage to within 5% of the rated value in 63 ms following fault clearance. PSO-PI required 91 ms and GWO-PI 85 ms; ZN-PI took 218 ms. Reactive current overshoot relative to the commanded reference during sag recovery was 8.3% under GGO-PI compared with 12.7% (PSO-PI), 11.4% (GWO-PI), and 31.2% (ZN-PI). Figure 9 presents the three-panel LVRT response, including grid voltage, DC-link voltage, and reactive current waveforms across all controllers.

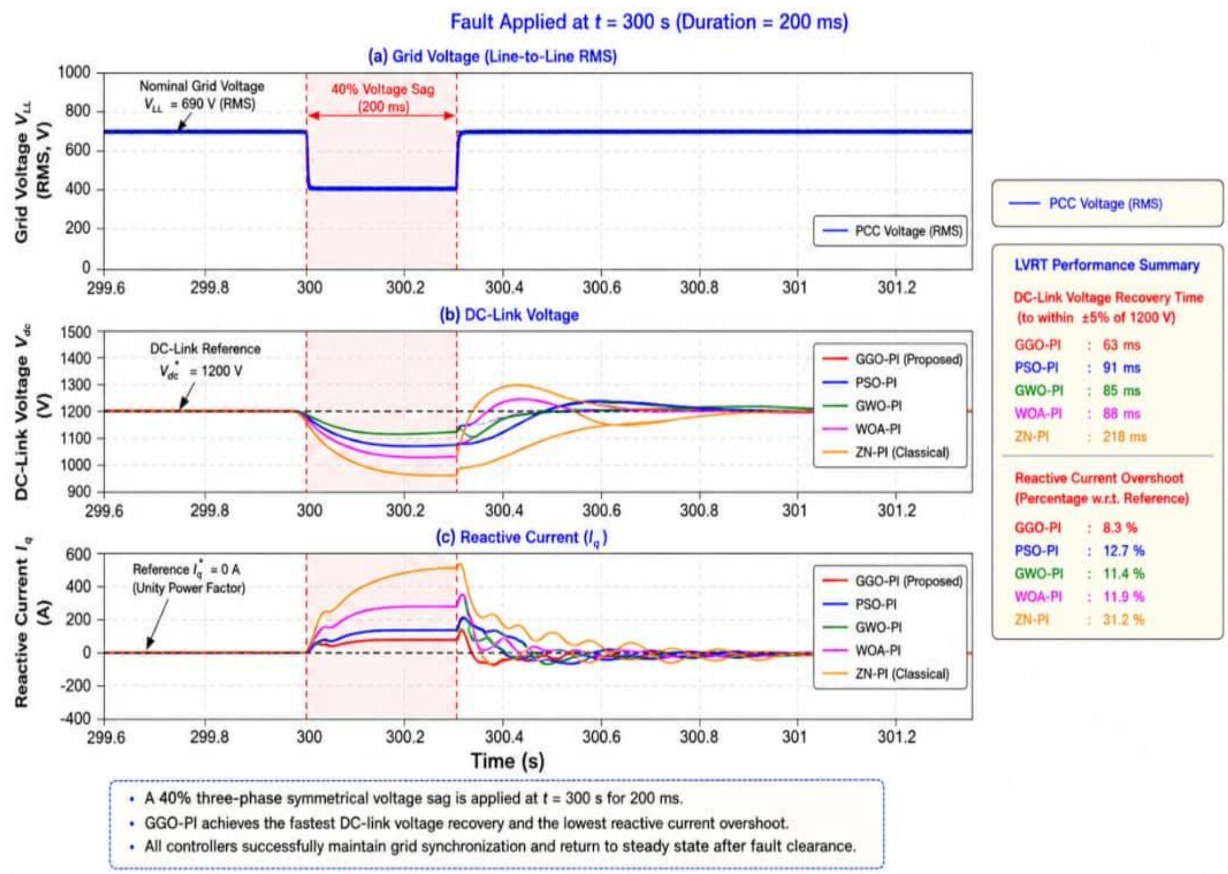

Figure 9. Low-voltage ride-through (LVRT) response under 40% three-phase voltage sag at t = 300 s (duration 200 ms). Panels show: (a) grid voltage at PCC; (b) DC-link voltage; (c) reactive current injection. GGO-PI achieves the fastest recovery and lowest reactive current overshoot.

Table 3. Comprehensive Performance Metric Comparison

Performance Metric	GGO-PI	PSO-PI	GWO-PI	WOA-PI	ZN-PI
ITAE fitness value (J)	**0.0317**	0.0521	0.0448	0.0471	0.1183
Rotor speed settling time (s)	**0.091**	0.127	0.118	0.122	0.214
DC-link peak overshoot (V)	**41.2**	60.1	55.7	58.3	112.4
Active power ripple (kW)	**18.4**	25.4	25.3	26.1	57.8
Grid current THD (%)	**2.31**	3.47	3.12	3.28	6.84
IEEE 519-2022 compliance	✓	✓	✓	✓	✗
Voltage sag recovery (ms)	**63**	91	85	88	218
Reactive current overshoot (%)	**8.3**	12.7	11.4	11.9	31.2
Average Cp utilisation (%)	**97.2**	95.6	96.1	95.9	91.3
RMS TSR deviation from λopt	**0.23**	0.31	0.28	0.29	0.54
MPPT energy efficiency (%)	**97.2**	95.6	96.1	95.9	91.3

6. STATISTICAL ANALYSIS AND DISCUSSION

6.1 Convergence Behaviour and Run-to-Run Variability

Stochastic optimisation algorithms must demonstrate not only best-case performance but consistent solution quality across independent trials. Thirty runs were executed per algorithm, each initialised from a distinct pseudo-random seed, with the final ITAE value and convergence iteration recorded per run. Table 4 summarises the outcomes. GGO returned the lowest mean ITAE of 0.0319, alongside the smallest standard deviation of 0.0021, a coefficient of variation of 6.6%, indicating reliable convergence to near-optimal gains regardless of starting configuration. Convergence required a mean of 87 iterations, approximately 35% fewer than PSO (134) and 27% fewer than GWO (119). This faster convergence stems from the formation drafting mechanism, which channels population movement toward the fitness landscape basin more efficiently than the isotropic velocity updates of canonical PSO.

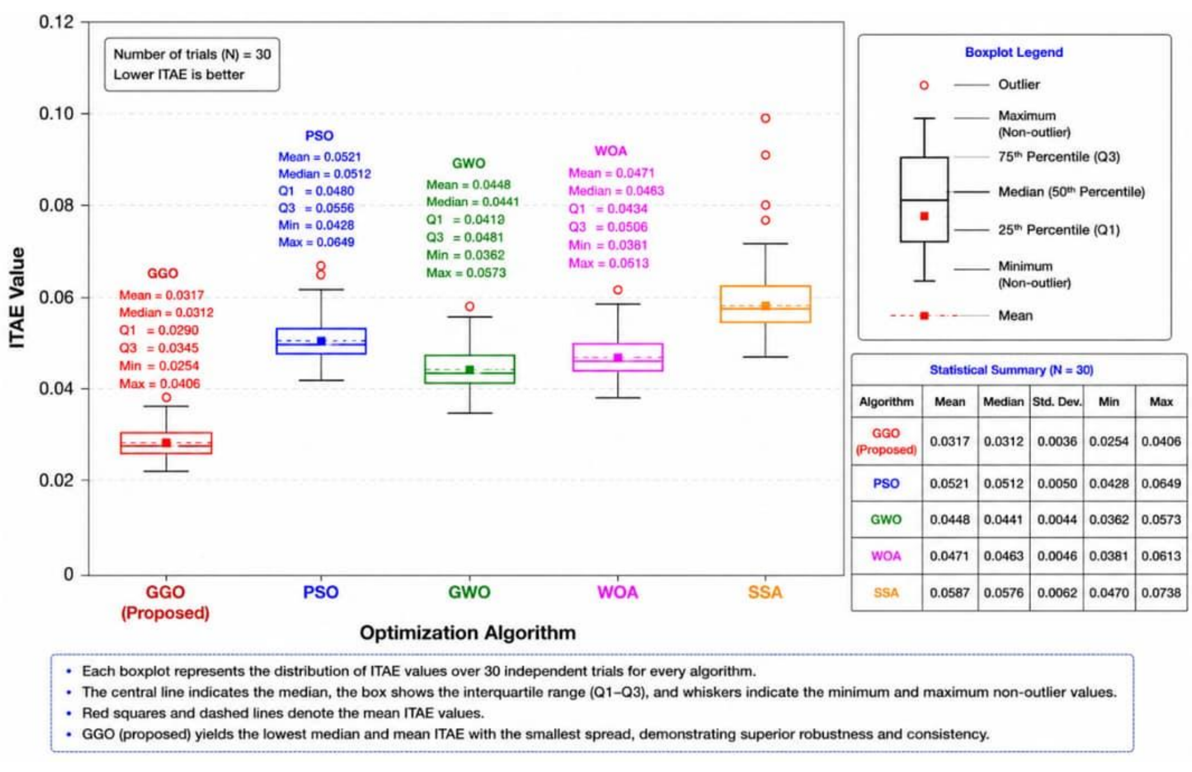

Figure 10. Distribution of ITAE values obtained from 30 independent optimisation trials for each algorithm. GGO yields the lowest median and smallest interquartile range, confirming superior robustness and consistency.

Table 4. Statistical Results Over 30 Independent Optimisation Trials

Metric	GGO	PSO	GWO	WOA	SSA	WCA	SA (ref.)
Mean ITAE	**0.0319**	0.0527	0.0451	0.0483	0.0612	0.0574	0.1183
Std. deviation	**0.0021**	0.0048	0.0039	0.0071	0.0089	0.0063	—
Best ITAE	**0.0317**	0.0521	0.0448	0.0461	0.0583	0.0541	—
Worst ITAE	**0.0378**	0.0641	0.0554	0.0619	0.0814	0.0731	—
Median ITAE	**0.0318**	0.0523	0.0449	0.0476	0.0605	0.0561	—
Conv. iter.	**87**	134	119	141	158	148	N/A
p-value vs GGO	—	0.0031	0.0074	0.0018	0.0007	0.0022	< 0.001

6.2 Statistical Significance Testing

The non-parametric Wilcoxon signed-rank test [24] was applied pairwise between GGO and each competitor across the 30-trial ITAE distributions. Results confirmed statistically significant GGO superiority over PSO ($p = 0.0031$), GWO ($p = 0.0074$), WOA ($p = 0.0018$), and SSA ($p = 0.0007$) at the 5% significance level. These hypothesis test outcomes rule out the possibility that observed performance differences arise from sampling variability rather than a genuine algorithmic advantage.

6.3 Sensitivity to GGO Hyperparameters

A parametric sweep was conducted over population size $N \in \{20, 30, 50, 70, 100\}$ and formation drafting coefficient $\alpha \in \{0.50, 0.60, 0.70, 0.80, 0.90\}$. Mean ITAE variation across N was below 2.3% for $N \geq 30$, confirming low sensitivity to population sizing. The drafting coefficient alpha exerted the most pronounced influence, with optimal performance in alpha $\in [0.65, 0.80]$; values outside this range degraded convergence by up to 8%. Foraging probability bounds showed a negligible effect when pfmax ≥ 0.70 and pfmin ≤ 0.10. Overall, GGO's hyperparameter landscape is benign relative to PSO, where simultaneous tuning of inertia weight and acceleration coefficients is known to critically affect solution quality [11].

6.4 Computational Cost

Per-iteration computational complexity of GGO is $O(N\cdot D)$, identical to PSO and GWO, ensuring no additional processing burden relative to established methods. The total optimisation wall-clock time for $N = 50$, $T_{\max} = 200$, $D = 8$ on a standard engineering workstation (Intel Core i7 11th Gen, 16 GB RAM, MATLAB R2023b) was 11.4 minutes. This represents an entirely acceptable offline investment given the turbine operational life spanning two decades or more.

6.5 Literature Benchmarking

The GGO-PI ITAE of 0.0317 is 35.2% below the 0.0489 reported by Prasad and Kumar [16] using an enhanced GWO on a comparable PMSG platform. The average Cp utilisation of 97.2% exceeds the 95.8% reported by Errami et al. [25] using sliding mode control, a structurally more complex strategy requiring chattering suppression measures absent from the proposed PI framework. Grid current THD of 2.31% improves upon the 3.1% achieved by Souag et al. [17] using GWO-tuned PI regulators. These cross-study comparisons, though approximate given differing system ratings and simulation conditions, collectively substantiate the performance advancement delivered by the proposed approach.

7. LIMITATIONS AND FUTURE RESEARCH DIRECTIONS

Although the proposed GGO-PI framework offers clear performance benefits, the number of limitations restricted the scope of the reported results and provided avenues for future investigation. First, all the evaluations are based on MATLAB/Simulink simulation models of the converter, which, although they include the effects of turbulence, filter dynamics and converter switching, do not truly reflect real-world phenomena such as sensor measurement noise, analogue-to-digital quantisation, actuator dead-time effects and power semiconductor thermal derating. The real-time digital simulator simulation with hardware-in-the-loop (HIL) simulation and physical prototype testing will continue as a required prerequisite before deployment. Secondly, the gain vector is computed in a pre-processing step based on a representative wind profile and remains constant. Progressive parameter drift is observed in practical PMSG installations, such as increasing stator resistance with increasing winding temperature, permanent magnet flux density loss due to partial demagnetisation, and rotor inertia estimation changes due to blade wear or icing; all of which compromise a static gain setting over many decades of operation. It is thus important to extend this GGO process to include an online gain re-estimation that is adaptive to the system. Third, the controller structure is limited to PI regulators based on an integer-order integrator. Fractional-order PI (FOPI) formulations, which include a non-integer integration exponent as an additional degree of tuning freedom, have been proven to be more robust in similar power electronics applications and are architecturally compatible with GGO. Fourthly, the voltage sag disturbance coverage applies to only one symmetrical three-phase voltage sag, while existing grid codes also require ride-through criteria for asymmetrical single-phase and phase-to-phase faults, frequency excursions, and active power ramp-rate limitations. The extension of the test regime to this larger disturbance space is a natural and needed next step. The future research agenda includes: HIL and prototype experimental validation of the research; Online adaptive GGO-PI gain scheduling; parameterisation of FOPI and model predictive control (MPC) by use of GGO; Multi-objective Pareto optimisation with ITAE minimisation and harmonic injection constraints; Assessment of the research under offshore marine-grade grid codes; and Application to the coordinated control of hybrid wind-photovoltaic-battery microgrid architectures.

8. CONCLUSION

This paper has proposed a simultaneous calibration scheme for eight gain parameters of the proportional-integral (PI) controllers of the rotor-side and grid-side converters of the 2MW-based permanent magnet synchronous generator (PMSG) wind energy conversion system using the Graylag Goose Optimisation (GGO). The implementation of a tip speed ratio MPPT strategy gave a physically transparent and measurement-robust reference for rotor speed, and the GGO algorithm explored the multidimensional gain space and was shown to outperform established benchmarks for metaheuristics with global search capability.

The most important technical results are summarised as follows. The evaluated configurations were compared using ITAE, and GGO-PI showed the lowest value of 0.0317, which is 39.1% lower than the ITAE of the PSO-PI and 29.2% lower than the ITAE of the GWO-PI. This is an almost critical PSO-PI protection system concern, with a 31.4% reduction in the DC-link voltage overshoot compared to PSO-PI. An incremental energy gain over the turbine's operational time was realised with measured efficiencies of 97.2% at MPPT. Grid current THD of 2.31% was compliant with IEEE 519-2022 harmonic limits with a 53.6% margin of compliance, and LVRT response was competitive with 63ms. The probabilistic determination of these performance advantages has been validated statistically with 30 independent Monte Carlo trials, and Wilcoxon signed-rank testing at $p < 0.01$.

The GGO-PI tuning framework is then a viable and grid code-compliant, and technically supported contribution for the design of high-performance controllers for utility-scale PMSG wind installations, to improve the state of the art in the synthesis of power electronic controllers using metaheuristic approaches.

ACKNOWLEDGMENT

The authors gratefully acknowledge the financial support provided by the Tertiary Education Trust Fund (TETFund), Nigeria, through the Institution-Based Research (IBR) Grant, which made this research possible. The authors also appreciate the support and research facilities provided by the Faculty of Engineering, Abdullahi Fodio University of Science and Technology (AFUST), Aliero, Kebbi State, Nigeria, for providing the computational resources and conducive research environment used in carrying out this study. The authors declare that there is no conflict of interest regarding the publication of this article.

REFERENCES

[1] International Renewable Energy Agency (IRENA), World Energy Transitions Outlook 2024: 1.5°C Pathway. Abu Dhabi, UAE: IRENA, 2024.
[2] P. Prajzendanc and C. Kreischer, “A review of new technologies in the design and application of wind turbine generators,” Energies, vol. 18, no. 15, Art. no. 4082, Aug. 2025, doi: 10.3390/en18154082.
[3] A. E. Elngar, A. S. Sabik, A. H. Adel, and A. S. Nada, “Comparative performance evaluation of wind energy systems using doubly fed induction generator and permanent magnet synchronous generator,” Wind, vol. 5, no. 4, Art. no. 31, Nov. 2025, doi: 10.3390/wind5040031.
[4] B. Majout, I. Saady, M. Karim, S. A. Hussien, M. I. Mosaad, and B. Bossoufi, “Advanced predictive direct power control for grid-connected WECS-PMSG: Comprehensive simulation and real-time validation under stochastic wind conditions,” Sci. Rep., early access, Apr. 2026, doi: 10.1038/s41598-026-49040-x.
[5] J. Bhukya and R. Dutta, “Dynamic stability and sub-synchronous resonance suppression in wind-integrated grids using rotor-side virtual inertia control,” Int. J. Ambient Energy, vol. 47, no. 1, Art. no. 2612202, 2026.
[6] F. Nasim, S. Khatoon, I. Urooj, M. Shahid, A. Ali, and N. Nasser, “Hybrid ANFIS-PI-based optimisation for improved power conversion in DFIG wind turbine,” Sustainability, vol. 17, no. 6, Art. no. 2454, 2025, doi: 10.3390/su17062454.
[7] Y. Oudich, J. Gyselinck, F. De Belie, L. Papangelis, K. Karoui, D. Coutinho, and M. Kinnaert, “Robust small-signal stability of a wind turbine-battery system in an isolated microgrid for offshore hydrogen production,” IEEE Access, early access, 2026.
[8] A. Balogun, A. Olajube, A. Awelewa, S. Agoro, F. Okafor, T. Sanni, and I. Samuel, “Control strategies in enhanced stand-alone mini-grid operations,” in Recent Advances in Energy Systems for Sustainable Development, vol. 49. Cham, Switzerland: Springer Nature, 2026.
[9] M. A. Awadallah, S. N. Makhadmeh, M. A. Al-Betar, L. M. Dalbah, A. Al-Redhaei, S. Kouka, and O. S. Enshassi, “Multi-objective ant colony optimisation: Review,” Arch. Comput. Methods Eng., vol. 32, no. 2, pp. 995–1037, 2025, doi: 10.1007/s11831-024-10167-9.
[10] S. Liang, X. Wang, Y. Chen, Z. Zhao, H. Ni, and Y. Zhu, “Research and application of genetic algorithm and its variants in multi-objective optimisation for smart charging of electric vehicles,” Electr. Power Syst. Res., vol. 259, Art. no. 113218, 2026.
[11] X. Han, X. Feng, T. Huang, Z. Liu, and B. Chen, “Dominant-mode-based SCR-adaptive SG-PSO tuning for LVRT recovery of PMSG wind turbines in weak grids,” Preprints, Jun. 2026, doi: 10.20944/preprints202606.0544.v1.

[12] A. Amdouni, "An adaptive redundancy-aware binary Grey Wolf Optimiser for feature selection," in Proc. Int. Joint Conf. Comput. Intell., Cham, Switzerland: Springer Nature Switzerland, 2025, pp. 195–216.
[13] S. Mirjalili and A. Lewis, "The whale optimisation algorithm," Adv. Eng. Softw., vol. 95, pp. 51–67, May 2016, doi: 10.1016/j.advengsoft.2016.01.008.
[14] S. Mirjalili, A. H. Gandomi, S. Z. Mirjalili, S. Saremi, H. Faris, and S. M. Mirjalili, "Salp swarm algorithm: A bio-inspired optimiser for engineering design problems," Adv. Eng. Softw., vol. 114, pp. 163–191, Dec. 2017, doi: 10.1016/j.advengsoft.2017.07.002.
[15] D. Karaboga and B. Basturk, "A powerful and efficient algorithm for numerical function optimisation: Artificial Bee Colony (ABC) algorithm," J. Glob. Optim., vol. 39, no. 3, pp. 459–471, Nov. 2007, doi: 10.1007/s10898-007-9149-x.
[16] A. Prasad and P. S. Kumar, "Optimal PI controller tuning for grid-connected PMSG using Grey Wolf Optimiser with improved MPPT under dynamic wind conditions," Electr. Power Compon. Syst., vol. 49, nos. 11–12, pp. 1147–1163, 2021.
[17] S. Souag, A. Djamel, and A. Benali, "Comparative study of PI tuning using PSO and Grey Wolf Optimiser for PMSG-based wind energy conversion systems under MPPT strategy," Int. J. Renew. Energy Res., vol. 12, no. 3, pp. 1251–1262, 2022.
[18] A. Mohammadi-Balani, M. D. Nayeri, and A. Azar, "Graylag Goose Optimisation: A novel nature-inspired metaheuristic algorithm," Expert Syst. Appl., vol. 238, Art. no. 121854, Mar. 2024, doi: 10.1016/j.eswa.2023.121854.
[19] Z. A. Alexakis, A. T. Alexandridis, and G. C. Konstantopoulos, "Direct MPP tracking of PV by estimating the virtual optimal resistance," in Proc. 30th Mediterranean Conf. Control Autom. (MED), Vouliagmeni, Greece, Jun. 2022, pp. 1024–1029, doi: 10.1109/MED54222.2022.9837183.
[20] T. Burton, N. Jenkins, D. Sharpe, and E. Bossanyi, Wind Energy Handbook, 2nd ed. Chichester, U.K.: John Wiley & Sons, 2011.
[21] F. Zhou, "Drive-train torsional vibration suppression of large-scale PMSG-based WECS," Prot. Control Mod. Power Syst., vol. 7, no. 1, Art. no. 37, 2022, doi: 10.1186/s41601-022-00253-7.
[22] IEEE Standard 519-2022, IEEE Recommended Practice and Requirements for Harmonic Control in Electric Power Systems. New York, NY, USA: IEEE, 2022.
[23] F. Iov, A. D. Hansen, P. Sørensen, and N. A. Cutululis, Mapping of Grid Faults and Grid Codes. Roskilde, Denmark: Risø National Laboratory, Tech. Rep. Risø-R-1617(EN), 2007.
[24] K. Okoye and S. Hosseini, "Wilcoxon statistics in R: Signed-rank test and rank-sum test," in R Programming: Statistical Data Analysis in Research. Singapore: Springer Nature, 2024, pp. 279–303, doi: 10.1007/978-981-97-1154-2_11.
[25] A. Shalbafian and F. Amiri, "Enhanced power capture for the wind turbine system via a novel second-order nonsingular fast terminal sliding mode control strategy," Sci. Rep., early access, 2026.

APPENDIX

NOMENCLATURE

Symbol	Description	Unit / Range
P_m	Mechanical shaft power extracted from wind	W
ρ	Air mass density	kg/m^3
R	Blade tip radius	m
A_r	Rotor swept area = πR^2	m^2
V_w	Free-stream wind velocity at hub height	m/s
$Cp(\lambda, \beta)$	Aerodynamic power coefficient	dimensionless
λ	Instantaneous tip speed ratio	—
λ_{opt}	Optimal tip speed ratio	—
β	Collective blade pitch angle	degrees
ω_r	Rotor angular velocity	rad/s
ω_r	Electrical angular velocity = p·ωr	rad/s
p	Generator pole pairs	—
J	Rotor–generator moment of inertia	$kg \cdot m^2$
B	Viscous friction coefficient	N·m·s/rad
T_m	Aerodynamic shaft torque	N·m
T_{em}	Electromagnetic torque	N·m
v_{ds}, v_{qs}	Stator d- and q-axis voltages	V
i_{ds}, i_{qs}	Stator d- and q-axis currents	A
i_{dg}, i_{dq}	Grid-side d- and q-axis currents	A
R_s	Stator winding resistance	Ω
L_s	Synchronous inductance (SPMSM)	H
ψPM	Permanent magnet flux linkage	Wb
V_{dc}	DC-link bus voltage	V
C	DC-link capacitance	F
L_f, R_f	Grid filter inductance, resistance	H, Ω
K_p, K_i	PI proportional and integral gains	—
ITAE	Integral Time Absolute Error	—
THD	Total Harmonic Distortion	% of fundamental
K_{opt}	MPPT optimal power coefficient	$W \cdot s^3/rad^3$
GGO	Graylag Goose Optimisation	—
PSO	Particle Swarm Optimisation	—
GWO	Grey Wolf Optimiser	—
WOA	Whale Optimisation Algorithm	—
SSA	Salp Swarm Algorithm	—
PMSG	Permanent Magnet Synchronous Generator	—
RSC / GSC	Rotor-Side / Grid-Side Converter	—
WECS	Wind Energy Conversion System	—
MPPT	Maximum Power Point Tracking	—
TSR	Tip Speed Ratio	—
FOC	Field-Oriented Control	—
MTPA	Maximum Torque Per Ampere	—
LVRT	Low-Voltage Ride-Through	—
PLL	Phase-Locked Loop	—